Self-Evolving Digital Twin-Based Online Health Monitoring of Multiphase Boost Converters

Kushan Choksi, *Graduate Student Member, IEEE*, Abdul Basit Mirza, *Graduate Student Member, IEEE*,
Austin Zhou, *Graduate Student Member, IEEE*, Deepi Singh, *Graduate Student Member, IEEE*,
Masayuki Hijikata, *Graduate Student Member, IEEE*, and Fang Luo, *Senior Member, IEEE*

***Abstract*—Component degradation in power electronic converters severely threatens the system's reliability. These components degrade over time due to switching action, and this phenomenon is further aggravated with wide band gap devices. For ensuring system reliability and accurate degraded component identification, the development of a real-time noninvasive health monitoring mechanism is desired. This article develops and validates a real-time digital twin (DT)-based condition monitoring for multiphase interleaved boost converters. The DT model is based on an actual state-space modeling approach which is solved numerically using Runge–Kutta fourth to mimic the physical system. Then, the output signals from physical hardware and the DT model are compared to find the least squared error-based multiobjective optimization problem. A metaheuristic approach like particle swarm optimization and genetic algorithm is used to estimate the health of components of the converter. The proposed methodology is extendable to different inductor coupling strategies under continuous-conduction-mode and discontinuous-conduction-mode operations. The idea is to generalize the DT modeling concept for condition monitoring. Moreover, the article proposes decoupling and hybrid approaches to improve estimation accuracy by 9.4% and reduce embedded computational requirements by 22%, respectively. A 75 kW, 60-kHz SiC IBC hardware prototype is built and tested for concept validation. Notably, the challenges and impact of various sensing integrity errors encountered during condition monitoring are also discussed. Finally, the article discusses novel pre and postprocessing steps for improving estimation accuracy and robustness in the case of control, sensing, and operating condition variability.**

***Index Terms*—Digital twin (DT), genetic algorithm (GA), interleaved boost converter (IBC), particle swarm optimization (PSO), quantization error, wide band gap (WBG).**

I. INTRODUCTION

Emergence of faster and more efficient wide band gap (WBG) technology, coinciding with the world's shift toward renewable energy solutions, have led to unprecedented demand for power electronic converters. However, performance gains achieved from faster switching of WBG come at the cost of major second-order concerns like electromagnetic interference (EMI), reflected wave, partial discharge, and communication interference [1]. These challenges have posed a significant question on the reliability of state-of-the-art converter technologies [2]. Power converter reliability is significantly impacted due to semiconductors and capacitors, as suggested in [2].

This has driven a paradigm shift in researchers' interest in condition monitoring and lifetime estimation. However, condition monitoring for power electronic components or systems is a nontrivial task due to increasing switching frequency. High switching frequency and higher dV/dt introduce second-order phenomena which greatly impact sensor integrity and embedded system communication and operation. The sampling frequency of sensors needed for such monitoring requires operating in higher frequency ranges from MHz to GHz [3]. This makes developing an accurate, robust, and reliable condition-monitoring algorithm a challenging task, unlike low-frequency power systems or mechanical digital twins (DTs) [4].

Degradation of power electronics converters is a slow process. Condition monitoring approaches serve as degradation or lifetime estimation indicators. Hence, the computational time of the algorithm is not a crucial factor in the presented application because the degradation of power electronic components occurs gradually, and therefore does not require time-critical computations [5]. Condition/health monitoring approaches can be classified mainly into component-level monitoring, system-level monitoring, and grid-level monitoring based on application nodes [5] and represented in Fig. 1. These approaches can be further subcategorized as online/offline monitoring based on monitoring continuity and time required. From the point of view of modeling philosophy, the algorithms can be a physics-based model, artificial intelligence-based model, noise injection-based model, or purely data-driven models [6], [7]. Lastly, condition monitoring can be invasive or noninvasive based on system interference. However, from the broader viewpoint of the power electronics domain; monitoring can be component- or system-level.

Manuscript received 21 March 2023; revised 2 July 2023; accepted 18 August 2023. Date of publication 4 September 2023; date of current version 23 October 2023. This work was supported in part by the Oak Ridge National Laboratory funded through the Department of Energy - Office of Electricity's Transformer Resilience and Advanced Components program led by the program manager Andre Pereira, and in part by the National Science Foundation NSF Award 1846917 and 1747757 (GR-19-08)) for lending financial support for this work. Recommended for publication by Associate Editor D. Qiu. *(Corresponding author: Kushan Choksi.)*

The authors are with the Electrical and Computer Engineering, Stony Brook University, Stony Brook, NY 11794-0701 USA (e-mail: choksi.kushan@stonybrook.edu; abdulbasit.mirza@stonybrook.edu; austin.zhou@stonybrook.edu; deepi.singh@stonybrook.edu; masayuki.hijikata@stonybrook.edu; fang.luo@stonybrook.edu).

Color versions of one or more figures in this article are available at https://doi.org/10.1109/TPEL.2023.3311710.

Digital Object Identifier 10.1109/TPEL.2023.3311710

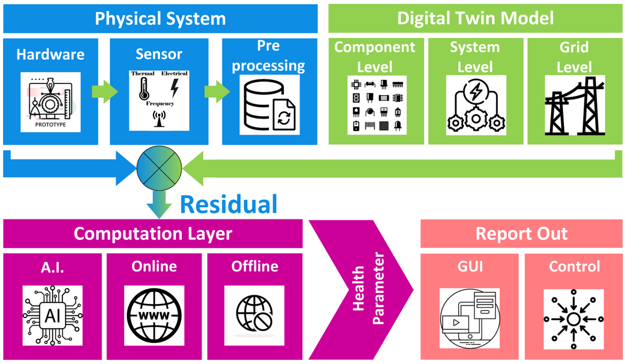

Fig. 1. Main scheme for DT-based condition monitoring.

Component-level monitoring refers to monitoring individual or a small number of related components using a separate circuit/model-based computation [7], while system-level monitoring involves simultaneous monitoring of multiple components using a combined architecture [6]. All condition/health monitoring techniques are mainly based on health indicators and respective measured signals. For instance, on-state voltages, on-state resistance [5], [8], [9], threshold voltages [9], Miller plateaus [10], case temperatures [11], [12], thermal resistance [2], [12], and other thermal parameters [13] are major health indicators for any semiconductor switch health monitoring [7]. Capacitor discharge voltage and current ripple indicate capacitor health, while inductor current ripple is used for inductor health monitoring. The component-level analysis is generally invasive and requires separate circuitry, while noninvasive data-driven and physics-based models are computationally complex [5].

Common health indicators for device monitoring are on-state resistance and device junction or case temperature. Thermal analysis-based monitoring is sensitive to sensor calibration and placement, which may not always be feasible [8], [13]. Frequency-based component monitoring methods are invasive, time-consuming, and costly due to high-frequency sensing requirements. In addition, they cannot differentiate power semiconductor degradation from other component degradation [10], [14], [15].

Offline system-level condition monitoring methods employing AI and artificial neural networks are suggested for monitoring capacitor [16] and power semiconductor [17] degradation but are limited by the cost of embedded design. Hence, system-level online model-based parameter identification methods have been proposed, leveraging the relationship between discretized transfer functions, degradation, output voltage, and duty cycle ratio [18]. Recursive least squares (RLS) [19] and Kalman filter (KF) [20] can be used to estimate transfer function coefficients. These algorithms are limited by the intricate mapping of transfer function coefficients to the converter's internal parameters and degradation. These methods are limited by the number of unknowns.

In summary, future power electronic systems require a noninvasive, calibration-free, memory-optimized, and adaptive condition monitoring approach. One promising solution is the use of DT-based approaches; a generic scheme for DT-based condition monitoring is represented in Fig. 1. DT creates a virtual representation of the physical system, continuously reflecting its behavior using real-time sensor data. The concept of basic power electronic DT modeling and monitoring is established in [5]. It employs solving state-space equations in real time for finding degradation for the dc–dc buck converter using control synchronization. However, Peng et al. [5] lacked sensitivity analysis based on control variation and extendability to other converter topologies. In [5], the estimated R_L and R_{dson} fluctuate in a large range. As R_L and R_{dson} have similar impacts on system signals, this method results in virtually indistinguishable estimations. The proposed methodology further decouples the R_L and R_{dson} estimation using a circuit signal path. This approach advocates estimating R_L during inductor discharging and R_{dson} estimation during inductor charging, improving the accuracy and precision of estimation by 9.4 % and 12 %, respectively.

State-of-the-art approaches are not extendable in terms of a topology or mode of operation; due to their embedded and memory optimization concerns. It also needs to account for practical concerns like sensor quantization, data synchronization error, topology extendability, and embedded circuit challenges. This article proposes a real-time, self-evolving adaptive DT methodology for future power converter applications. Along with DT being noninvasive and calibration-free, the proposed DT characteristics of adaptive and self-evolving condition monitoring are described as follows.

1) *Modularity and Extendability:* The methodology must be modular so that it can be extended to variants of the same physical system (e.g., boost converter, interleaved boost converter (IBC), and IBC with different coupling strategies/layout-based parasitic coupling).
2) *Self Calibrating:* Multiobjective optimization used for condition monitoring must have self-tuning ability based on various sensor integrity and small signal noise.
3) *Operating Variation Adaptability:* Adaptive modeling to changes with operating points or control variation.
4) *Degradation Immunity:* Modeling should not depend on preset values of circuit parameters but should adapt to the degradation of components.

This article proposes an embedded processor-based DT for real-time ($\leq$ 1 min) health estimation of a multiphase IBC with various inductor coupling strategies. The proposed design can simulate the behavior of its real-world counterpart using a state-space model, solved using the Runge–Kutta (RK) fourth-order numerical method [21]. This information, in addition to sensor data (channel current, output voltage) is used to find a squared error objective function. This objective function is minimized to solve the metaheuristic multiobjective optimization problems using particle swarm optimization (PSO) and genetic algorithm (GA) algorithms. The solution to this optimization is then mapped to the health of the component. Lastly, the proposed modeling employs error tuning, synchronization, and a power initialization stage to ensure the adaptable and self-evolving nature of condition monitoring.

A. *Contribution of the Paper*

This article aims to provide a noninvasive, calibration-free, memory-optimized, expandable, and adaptive condition monitoring approach. Part of the methodology of this article has been presented in [6], which mainly discussed the general idea of the proposed DT-based condition monitoring approach for a two-phase IBC. In addition to [6], this article has an extended methodology for N-phase IBC with the coupled inductor. Further, experimental validation is provided for establishing the relationship of the proposed method estimation accuracy with component variation, sampling frequency, and sensing errors. The major contributions of this article are as follows.

1) This article provides complete discretized state-space modeling of an N-phase coupled IBC.
2) Proposed condition monitoring utilizes PSO and GA for minimizing the square error between the DT model and actual hardware signals, for simultaneous parameter estimation. The optimization weights are autotuned to compensate for the sensor integrity issued.
3) The proposed decoupling approach for decoupling estimation of R_L and R_{dson}, which aids in improving accuracy and precision of estimation by 9.4 % and 12 %, respectively, as compared to averaging approach provided in [5] and [6].
4) This article provides hardware validation using a 75-kW four-phase IBC with reverse coupled inductors for rigorous accuracy analysis of proposed DT.
5) The article provides the impact of sensor integrity, embedded design constraint, and component variation on the performance of DT. Adaptive postprocessing includes sensor error compensation and power initialization for improved robustness of estimation.
6) The article provides practical insights on methodology optimization and sensitivity for extendable implementation. The proposed hybrid approach aids in reducing embedded design cost and robustness of estimation.
7) This article provides a graphical user interface-based report-out strategy by using a low-cost DSP [22].

B. *Organization of the Paper*

The rest of this article is organized as follows. First, Section II discusses the DT modeling of a two-phase boost converter, sampling, and control circuit. The extendability of modeling to a multiphase boost converter, sustainable for different coupling strategies and modes of operation, is established. Second, Section III deals with metaheuristic optimization formulation for DT-based condition monitoring. In addition, Section IV lays out the hardware evaluation setup, embedded design consideration, and rigorous hardware validation. The impact of sensor integrity and component variation on the robustness of the proposed DT performance is studied in detail. Section V provides practical insights into the explicit implementation of adaptive DT-based condition monitoring from aspects of switching frequency, type of converter, type of sensor, and embedded design platform. Finally, Section VI concludes this article.

II. SYSTEM MODELING: ADAPTIVE DIGITAL TWINING

The DT virtually replicates the physical converter, which can be used to estimate the component values by matching the response of the DT to that of the actual hardware. The main idea of DT-based condition monitoring is thoroughly represented in Fig. 2. The major components of the proposed methodology are broadly classified as follows.

1) *Physical System:* A 75-kW, multiphase IBC with reverse coupled inductors is used for the proposed methodology.
2) *Sensors:* This is the most crucial part of the DT approach. It passes vital information about the physical world to the DT model. For instance, the channel current sensor and output voltage sensor.
3) *DT Model:* Proposed methodology uses a state-space model solved using the RK fourth-order method to mirror/replicate the physical system.
4) *Data and Analytics:* Once the sensor and the DT model provide data, this data must be utilized to extract crucial insights. Health parameters using nature-inspired multiobjective optimization.
5) *Reporting Actuation:* The proposed methodology reports health estimations to the user and maintenance team for protection.

As discussed earlier, this article models a multiphase IBC with reverse coupled inductors, as suggested in Fig. 3. IBC topologies for high-power applications are gaining attention due to several interleaving benefits: modularity, high power, and reliability [6]. Moreover, coupled IBC reduce EMI, ripple, improve efficiency, and reduce filter size [23]. The modeling of a physical system is provided in the following subsection.

A. *Modeling of Two-Phase Interleaved Boost Converter*

In literature, [24], [25], details were provided for modeling of dual IBCs. In addition, an extendable multiphase IBC model was provided in [26], but this work lacks consideration of parasitics like R_L, R_{ON}, and R_c in the derivation of the multiphase IBC. This article illustrates the state-space modeling of the multiphase reverse coupled IBC, including all its parasitics. The output current is distributed in a number of phases (N), aiding with reduced current stress in each switch, switching at frequency f_{sw}. Moreover, the phase difference between consecutive channels is $\phi = 360^{\circ}/N$. Notably, coupling and increased phases of IBC lead to an increased number of subintervals in operation mode modeling of IBC making modeling a nontrivial task to model both CCM and DCM modes. First, a model of a two-phase IBC with coupled inductors is derived; later, the extendability of the modeling approach is discussed in detail for the family of multiphase boost IBC, as even-phase IBCs are modular, with each building block being a two-phase IBC.

Fig. 3 illustrates the schematic of a two-phase IBC with reverse coupled inductors. Here, $i_{L\{1,2\}}$ and v_C represent the inductor channel currents and the output capacitor voltage. Similarly, $R_{L\{1,2\}}$, $R_{ON\{1,2\}}$, and R_c are the parasitic resistances of the coupled inductors, switches, and output capacitor, respectively. The two inductors are assumed to be equal $L_{\{1,2\}} = L$.

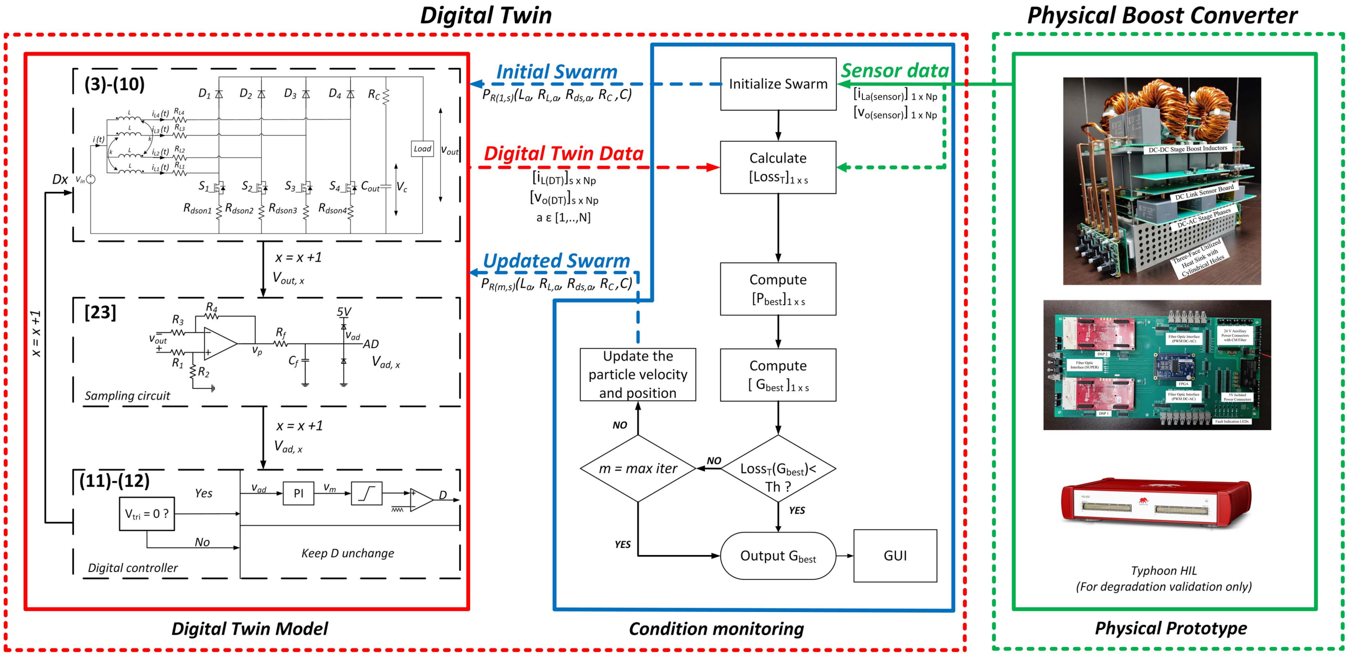

Fig. 2. Detailed flow chart of proposed DT-based condition monitoring.

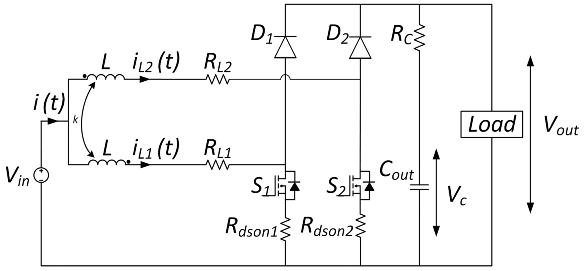

Fig. 3. Two-phase interleaved boost converter with reverse coupled inductor.

Notably, R_{ON} represents switching loop ON resistance, it includes $R_{ds,ON}$, and interconnect and PCB trace resistances R_{stray}. The coupling coefficient and the equivalent mutual coupling are considered as $k \,\epsilon\, (-1, 1)$ and M, respectively. Notably, this modeling is only valid for k value approaching 1 or -1, but not at the exact value 1 or -1. Also, all equations will represent inductors as L and the load resistance as R. The output capacitor is defined as C.

The MOSFET (S_1) status is represented with a binary variable. The MOSFET is ON when $s_1 = 1$ and the MOSFET is OFF when $\bar{s_1} = 1$. Similarly, the switching state of the two-phase IBC can be represented with a pair of binary variables $s_1 s_2$, as referred in (12) and explained in Section II-B. Hence, the four possible switching states are $\bar{s_1}\bar{s_2}$, $\bar{s_1}s_2$, $s_1\bar{s_2}$, and $s_1 s_2$, as shown in Fig. 3, The schematic illustrates the switching combinations as $S_1 - D_2$, $D_1 - D_2$, $S_2 - D_1$, and $S_1 - S_2$.

$$k = \frac{M}{\sqrt{L_1 * L_2}} = \frac{M}{\sqrt{L * L}} = \frac{M}{L} \tag{1}$$

$$K_c = (1 - k^2)L. \tag{2}$$

The DT representation in this proposal is based on discretizing the state variables' response and on piecewise differential equations. This requires the DT to model both the transient and steady-state responses. The transient response is sensitive to the values of the passive components, such as L and C. To cater to this, the actual state-space model is given as follows:

$$\dot{x}(t) = Ax(t) + Bu(t) \tag{3}$$

$$\dot{x}(t) = \begin{bmatrix} \frac{di_{L_1}}{dt} \\ \frac{di_{L_2}}{dt} \\ \frac{dv_c}{dt} \end{bmatrix}, x(t) = \begin{bmatrix} i_{L_1} \\ i_{L_2} \\ v_C \end{bmatrix}, U(t) = \begin{bmatrix} V_{in} \\ V_d \end{bmatrix} \tag{4}$$

$$StateMatrix : A =$$

$$\begin{bmatrix} \frac{-[G_1+\bar{s_1}\bar{s_2}Pk]}{K_c} & \frac{-[kG_2+\bar{s_1}\bar{s_2}P]}{K_c} & \frac{-P[\bar{s_1}+\bar{s_2}k]}{K_cR} \\ \frac{-[kG_1+\bar{s_1}\bar{s_2}P]}{K_c} & \frac{-[G_2+\bar{s_1}\bar{s_2}Pk]}{K_c} & \frac{-P[\bar{s_2}+\bar{s_1}k]}{K_cR} \\ \frac{\bar{s_1}}{C}\left[\frac{R}{R+R_c}\right] & \frac{\bar{s_2}}{C}\left[\frac{R}{R+R_c}\right] & \frac{\bar{-1}}{C}\left[\frac{1}{R+R_c}\right] \end{bmatrix} \tag{5}$$

$$\text{Input Matrix:}B = \begin{bmatrix} \frac{1+k}{K_c} & \frac{-1}{K_c}(\bar{s_1}k + \bar{s_2}) \\ \frac{1+k}{K_c} & \frac{-1}{K_c}(\bar{s_2}k + \bar{s_1}) \\ 0 & 0 \end{bmatrix} \tag{6}$$

$$\text{where } P = \frac{RR_C}{R + R_c} \tag{7}$$

$$\underset{i \in [1,2,\ldots,N]}{G_i} = R_{Li} + s_i R_{ONi} + \bar{s}_i P. \tag{8}$$

Here, (4)–(6) define states vector, state/system matrix, and input matrix, respectively. Stability and natural response characteristics of a continuous linear time-invariant (LTI) system (i.e., piecewise linear with states and time in this case) can be studied from the eigenvalues of the matrix A. Notably, the state-space model developed is valid for both the discontinuous-conduction-mode (DCM) and the continuous-conduction-mode (CCM) operation due to its linking with s_1, s_2. In addition, it is extendable to all subintervals of an N-phase boost converter. This derivation, as suggested in (3)–(8), considers all the parasitic and inductor coupling strategies. Lastly, it is extendable with increasing parallel phases in the boost converter family. It is explained in detail in the next Section II-A1

1) Extended Derivation for Multiphase IBC Converter: The state-space equation, as suggested above, can be extended for any multiphase model with different coupling strategies. The generic multiphase IBC state-space model proposed is as suggested in (25)–(27). Also, the different coupling strategies from literature have been illustrated in Fig. 12. It shall be noted that this modeling is generic for any boost converter, IBC, coupled IBC, or reverse coupled IBC operation in CCM or DCM modes of operation.

The variable G_i refers to the decoupled self-inductor states of any phase leg, as suggested in (8), whereas $H_{m,n}$ refers to the impact of other phases on the state variable of that phase leg given in (25). The modified state/system matrix and input matrix are constructed using G_i and $H_{m,n}$, as given in (26) and (27). The idea of generic IBC assumes that the coupling coefficient between the phase inductors is known, and the value of coupling coefficient k is used in derivation to determine redundant terms of (25)–(27), such that $k_{i,j}$ refers to coupling coefficient between the *i*th phase leg and the *j*th phase leg, respectively.

This article linearizes the differential equation using the numerical RK fourth-order method [21], as discussed in Section II-A2. The eigenvalue-based generic solutions can also be derived for solving the same set of equations. However, it is computationally more intensive, as suggested in [5].

2) Solving State Space Model: A typical fourth-order RK method for linearizing two-phase IBC DT model (3)–(8) is used, as suggested in [21]. The RK state function can be represented as follows:

$$\begin{cases} f_1(i_{L_1}, i_{L_2}, v_c) = \frac{di_{L_1}}{dt} \\ f_2(i_{L_1}, i_{L_2}, v_c) = \frac{di_{L_2}}{dt} \\ f_3(i_{L1}, i_{L2}, v_c) = \frac{di_{v_c}}{dt}. \end{cases} \tag{9}$$

It shall be noted that capacitor voltage v_C and output voltage V_o are different; the measured value from the sensor will always be V_o. Hence, v_c can be derived using (10) along with (9)

$$V_{o,x} = P[\bar{s_1} i_{L_1,x} + \bar{s_2} i_{L_2,x}] + \frac{P v_{c,x}}{R_c}. \tag{10}$$

The RK method used for finding the next state values of the state variables ($i_{L1,x+1}, i_{L2,x+1}$, and $v_{c,x+1}$) is expressed in [21]. The subscript x represents the current sample, whereas the following sample will use subscript $x+1$. The time step between them is defined by h. The basic equation for obtaining the above states is clearly described in [21].

The RK method is solved considering the knowledge about seven circuit parameters ($L_{\{1,2\}}$, $R_{L\{1,2\}}$, $R_{ON\{1,2\}}$, and R_c), which will be obtained from metaheuristic optimization in each iteration, as explained later in Section III-A.

Hence, this would commence the modeling of DT, if control modulation signals are available to the DT model. It will become necessary to model and solve the controller inside DT if a control decoupled condition monitoring system is required, as suggested in the following Section II-B.

B. Modeling of Control and Sampling Circuit

The RK state-space solution needs to be control adaptable. This article obtains modulation signal V_{mod}, by modeling a closed-loop PI controller inside DT. The linearized controller is expressed in (11) and solved using a numerical method. i.e., RK fourth order. This article obtains modulation signal V_{mod}, using PI controller proportional and integral coefficient K_P and K_I. Voltage error V_e computed using V_{ref} and normalized measured voltage V_{mod}.

$$\begin{cases} V_{e,x} = V_{\text{ref}} - V_{\text{mod},x} \\ V_{\text{mod},x+1} = V_{\text{mod},x} + K_P(V_{e,x+1} - V_{e,x}) + K_I h V_{e,x+1}). \end{cases} \tag{11}$$

The switching state for phase leg 1 can be represented using s_1 and derived as follows:

$$s_{1,x+1} = \begin{cases} 1, if\ (V_{\text{mod},x+1} \geq= V_{tri_1,x+1}) \\ 0, if\ (V_{\text{mod},x+1} <= V_{tri_1,x+1}). \end{cases} \tag{12}$$

Once the switching states are derived, the last part of DT is to synchronize the experimental data with DT model output signals. This will need modeling of the sampling circuit to estimate $V_{ad,x}$, which is the sampling circuit output. The sampling circuit is a simple low pass amplifier-based RC network, which is again estimated using the RK fourth-order method, as suggested in [6] and Section II-A2.

III. DIGITAL TWINNING FOR METAHEURISTIC OPTIMIZATION-BASED CONDITION MONITORING

The DT model of the two-phase IBC is developed using (3)–(8). It is imperative to note that (9) involves highly nonlinear functions with seven unknown variables ($L_{\{1,2\}}$, $R_{L\{1,2\}}$, $R_{ON\{1,2\}}$, and R_c). Traditional algorithms like the Kalman filter cannot estimate parameter health with fewer known than unknowns. The extended Kalman filter is unstable due to linearization and is computationally intensive with large matrixes [27]. Gradient descent and heuristic approaches are complex, memory-intensive, and computationally intensive, but they provide enhanced accuracy through deterministic estimation [28].

A. Optimization Formulation

This article employs metaheuristic evolutionary algorithms like PSO and GA to overcome the abovementioned challenges. Health/condition monitoring can be performed by matching the response of DT signals (as obtained from Section II-A2) with that of the actual IBC converter. A least squared error (LSE)-based multiobjective optimization problem can be formulated, as in (13)–(15). Each signal can be used as a separate objective function or combined. The LSE for channel currents and output voltage for the number of data points(N_p) is given as

$$\begin{cases}\text{LSE}_{I_L}(x) = \frac{1}{N_p}\sum_{a=1}^{N}\sum_{b=1}^{N_p}(i^b_{La(DT)} - i^b_{La(\text{sensor})})^2\\ \text{LSE}_{V_o}(x) = \frac{1}{N_p}\sum_{b=1}^{N_p}(V^b_{o(DT)} - V^b_{o(\text{sensor})})^2\end{cases}\tag{13}$$

where, $i_{L(\text{sensor})}$ and $V_{o(\text{sensor})}$ are data collected from the physical sensors. Similarly, $i_{L(DT)}$ and $V_{o(DT)}$ are data collected from the DT model, as suggested in Fig. 2. Also, N is the number of phase legs, and N_p is the number of points.

The multiobjective optimization for N phase IBC hence can be given by

$$\underset{\substack{[L_a,R_{La},R_{ON,a},R_C,C]\\ a\epsilon[1,2,\ldots,N]}}{\text{minimize}}\ \text{Loss}_T = \alpha_a\text{LSE}_{ILa} + \beta\text{LSE}_{V_o}\tag{14}$$

$$\text{constraints}: -\begin{cases}L_{\min} < L_a < L_{\max}\\ R_{La,\min} < R_{La} < R_{La,\max}\\ R_{ONa,\min} < R_{ONa} < R_{ONa,\max}\\ R_{C,\min} < R_C < R_{C,\max}\\ C_{\min} < C < C_{\max}\end{cases}\tag{15}$$

where α_a and β are corresponding weights for tuning objective function.

It is worth mentioning that this optimization formulation is relevant to any multiphase IBC, irrespective of coupling or mode of operation. This is a multiobjective optimization minimizing Loss_T over parameter P_R that includes L_a, R_{La}, lumped device on resistance $R_{ON,a}$, R_C, and C, where subscript a refers to the phase leg. The state-space model, as suggested in (3)–(8), is a piecewise linear function that satisfies Lipschitz continuity [29], meaning the slopes of the linear segments are bounded, it can help convergence. This optimization formulation consists of the least square error of a piecewise linear equation; hence it is a convex optimization function, as suggested in [30].

This article uses metaheuristic optimization, as explained in the next section. The problem was solved using PSO [31] and GA [32]. However, for the sake of simplicity and intuitiveness, only the PSO algorithm is discussed for understanding the flow of condition monitoring. PSO is a population-based iterative optimization algorithm that replicates the swarm behavior in fish schooling or birds flocking to guide the particles to search for the globally optimal solutions [31].

B. *Flow of Condition Monitoring Optimization*

The methodology of the proposed DT-based condition monitoring method is shown in Fig. 2, it includes three basic components as follows.

1) *DT Model:* Digital replica of the physical system.
2) *Physical System:* 75-kW, four-phase IBC with reverse coupled boost inductors, as suggested in Fig. 4.
3) *Analytical Interface:* PSO and GA-based multiobjective optimization-based condition monitoring.

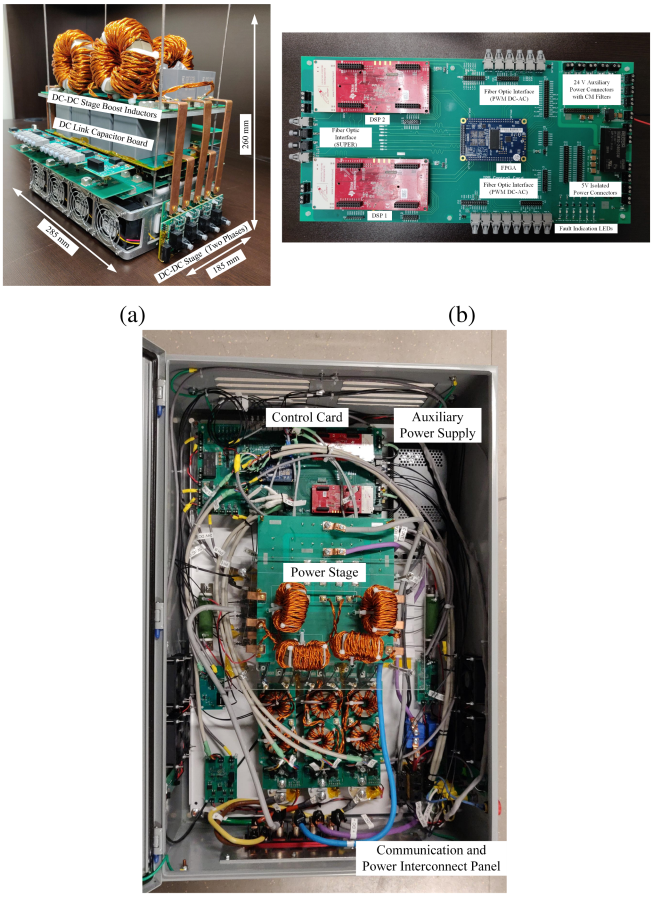

(a) (b)

(c)

Fig. 4. 75-kVA two-stage converter. (a) DC–DC stage. (b) Control card. (c) Final NEMA box assembly.

The DT-based condition monitoring algorithm initiates by collecting sensor data $[i_{La(\text{sensor})}]_{(1\times N_p)}$ and $[V_{o(\text{sensor})}]_{(1\times N_p)}$ such that $a\epsilon[1, 2, \ldots, N]$ and N_p is the number of data points. Here, the number of parallel boost channels is $N = 4$. Further, the population of parameter P_R is randomly generated based on swarm size (s). P_R includes L_a, $R_{L,a}$, lumped on resistance $R_{ON,a}$, R_C, and C; in other words, the circuit components are subjected to metaheuristic condition monitoring. This is used to generate $[i_{La(DT)}]_{(s\times N_p)}$ and $[V_{o(\text{sensor})}]_{(s\times N_p)}$ using DT model (3)–(8). Now that data are collected from both the physical and digital systems, the data are used to compute objective functions for optimization of $[\text{Loss}_T]_{(s\times 1)}$.

The values of $[\text{Loss}_T]$ for s particles are sorted in increasing order, and the P_R associating the minimum value of $[\text{Loss}_T]$ amongst the entire swarm is stored as global best (G_{best}). Also, the P_R associating the minimum value of $[\text{Loss}_T]$ for each particle over maxiter iteration is stored as personal best (P_{best}) for the particle. Now if G_{best} does not meet the convergence criteria, the value of particles is updated using velocity vector V

$$\begin{cases}V_{m,n} = \lambda_{m-1}V_{m-1,n} + 2\gamma_{1m-1,n}(G_{best} - P_{m-1,n})\\ \qquad +2\gamma_{2m-1,n}(P_{best} - P_{m-1,n})\\ P_{Rm,n} = P_{Rm-1,n} + V_{m,n}\end{cases}\tag{16}$$

where n and m are the numbers of particles and iterations, respectively. Such that n and m according to s and the number of parameters to be optimized. Furthermore, λ, γ_1, and γ_2 are

TABLE I
IPS SPECIFICATIONS

Stage	DC–DC	DC–AC
V_{in}(V)	500–800	800
$V_{ac,\text{line}}$ RMS (V)	800	480
Switching Frequency (kHz)	60	30
Device Per Position	1	2
SiC MOSFET	CREE C3M0016120D	
SiC Schottky Diode	Onsemi FFSH50120A	

learning rate, global best weight, and personal best weight, respectively. These values are set based on suggestions in [31].

The same flow is iterated until G_{best} meets the convergence criteria [error threshold (Th)]. The values of G_{best} are then reported as the final health of the component, as shown in Fig. 2.

IV. EXPERIMENTAL VALIDATION: DT-BASED CONDITION MONITORING

The experimental verification for the DT-based condition monitoring is performed on a 75-kVA two-stage grid-tied converter, shown in Fig. 4. The specification of the same is, as listed in Table I and explained in detail in [33]. The dc–dc stage consists of a synchronous four-phase interleaved boost converter with reverse coupled inductors, as suggested in Fig. 12. The dc–ac stage has a two-level split-phase inverter (2L-SP) topology with SPWM.

The converter is assembled on a 3-D platform using a three-faced utilized heat sink [34]. The dc–dc stage assembly is divided into two parts, each with two phases, on one side of the heat sink. Meanwhile, the dc–ac stage is positioned on the top side of the heat sink, with the dc link capacitor PCB placed on top. Copper tabs are used to interface the dc link board with the dc–dc and dc–ac PCBs. The dc–dc–ac stage can function solely as a dc–dc stage, with both coupled and uncoupled inductor structures, by adjusting the placement angle by 90°, as shown in Fig. 4, or dc–ac stage can be operated as simple 2L or 2L-SP.

To validate the concept, the dc–dc stage is tested standalone with a resistive load connected to the dc link, while the dc–ac stage is disconnected. This ensures the suppression of potential switching noise/harmonics from the dc–ac stage. Robustness is evaluated by loading the dc–dc stage with the dc–ac stage connected to an *R-L* load. No variations were observed in both cases. Therefore, the discussion focuses solely on the standalone testing of the dc–dc stage for simplicity.

A. Embedded System Design: DT Perspective

The control card integrates power to gate drivers, sensors, and control circuits [Fig. 4(c)]. It consists of two LAUNCHXL-F28379D DSPs and a DE-0 Nano Cyclone IV FPGA. The DSPs and FPGA communicate via SPI. The DSP handles core/supervisory tasks and reports condition monitoring results. An FPGA-based UART communication path enables transparent DT access to an external user interface, as suggested in Appendix A. The key details for DT implementation on a DSP are explained in Section V-G.

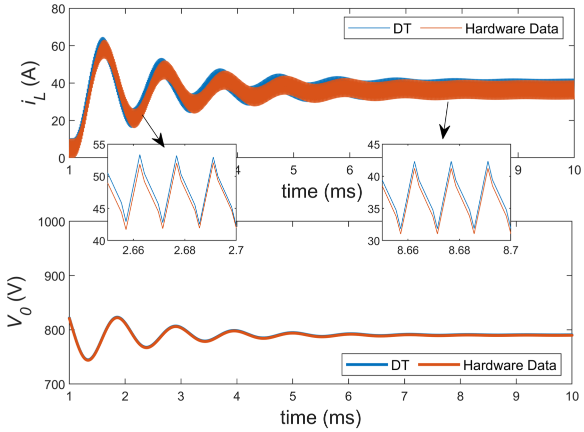

Fig. 5. DT performance: coupled case.

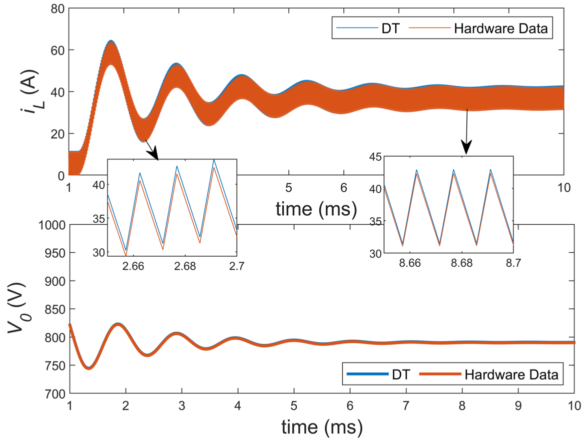

Fig. 6. DT performance: uncoupled case.

B. Sensing Architecture Design

DT-based health monitoring accuracy relies on acquiring noise-free data from high-bandwidth voltage and current sensors. Texas Instrument's AMC1302x series optically isolated amplifiers with a bandwidth of up to 800 kHz (≥ 10 times switching frequency) are chosen for low-cost shunt current measurements. Broadcom's ACNT-H790-500E isolated differential amplifier, housed in a stretched SSO-8 package, is selected for voltage sensing. Both sensors are connected to the control card, and the shield is grounded on both sides for external E and H-field shielding.

C. DT Modeling Performance

The DT modeling performance can be assessed by comparing the values of i_L and V_o between the DT model converter (3)–(8) and the physical system, as suggested in Figs. 5 and 6. It is evident that the waveforms from the DT and the physical system approximately overlap in both coupled inductor IBC and

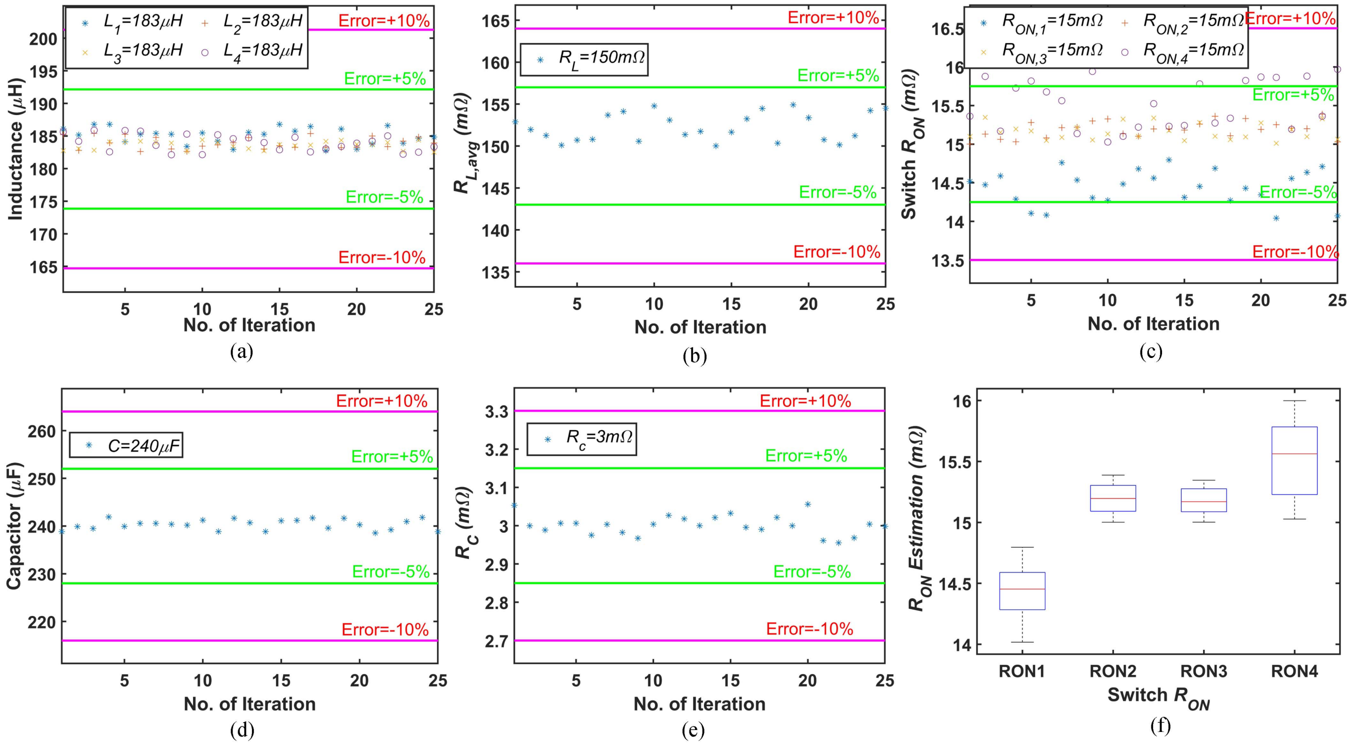

Fig. 7. Parameter estimation of Table II. (a) $L_{1,2,3,4}$. (b) R_L. (c) Lumped device on resistance $R_{ON,1,2,3,4}$. (d) C. (e) R_C. (f) Boxplot analysis of lumped device on resistance $R_{ON,1,2,3,4}$. It shall be noted that all the subplots denote ±5% and ±10% error bands in green and pink, respectively.

TABLE II
ACTUAL PARAMETER FOR EXPERIMENTAL VALIDATION

Phase Leg	Actual Values of Parameter				
	L (μH)	R_L (mΩ)	R_{ON} (mΩ)	R_C (mΩ)	C (μF)
1	183	147	15	3	240
2	182	148	15		
3	184	150	15		
4	183	151	15		

uncoupled inductor IBC. This ensures minimum Loss$_T$ [in (13)] under normal operation; which in turn establishes a strong base for the estimated parameters' accuracy by the proposed method.

It was observed that the coupled case of the DT model provides lesser accuracy during the transient state of IBC than uncoupled case. Hence, it is best for estimation accuracy to start when the converter comes into a steady state. Lastly, as it can be observed from Fig. 5, the Loss$_T$ computation is highly dependent on time instant, steady, or transient state. Hence, it is in the best interest to average the parameter estimation over multiple convergences of condition monitoring algorithms to achieve the robustness of the solution.

D. Digital Twin: Parameter Identification

The four-phase IBC validation used circuit parameter values from Table II. L, R_L, R_C, and C were extracted using an impedance analyzer. R_{ON} magnitude was obtained from the device datasheet [35], considering the operating condition. A thermocouple near the device provided an estimation of the junction temperature, used to validate DT's R_{ON} estimation. R_{ON} variation indirectly indicates device current or gate voltage changes, such as failures in paralleled devices or reduced effective gate voltage. The proposed DT signifies anomalies in device operation, though it does not precisely predict fault types. Parameter identification of the DT was experimentally validated with 1000 iterations for convergence. However, some results show 25 iterations for easier visualization.

The parameter identification using the proposed DT is presented in Fig. 7. It is important to note that for Fig. 7, each health estimation iteration utilized a dataset comprising 20 switching cycles under steady-state conditions. This article emphasizes parameter identification exclusively during steady-state operation. Notably, when parameter identification relied solely on transient state data, the accuracy of health estimation decreased. This decline in accuracy was attributed to the fluctuating operating conditions and parasitic behavior, resulting in increased errors, as demonstrated in Figs. 5 and 6.

The accuracy of DT estimation is as high as 97.2%, 98.6%, and 96.8% for $L_{1,2,3,4}$, C, and R_C, respectively. However, the estimation accuracy is reduced for $R_{L,1,2,3,4}$ and $R_{ON,1,2,3,4}$; accuracy of estimation is as low as 86.1% and 79.8%, respectively. If estimated using only transient state data the accuracy for $L_{1,2,3,4}$, C, and R_C was observed to be 95.8%, 98.1%, and 86.2% respectively.

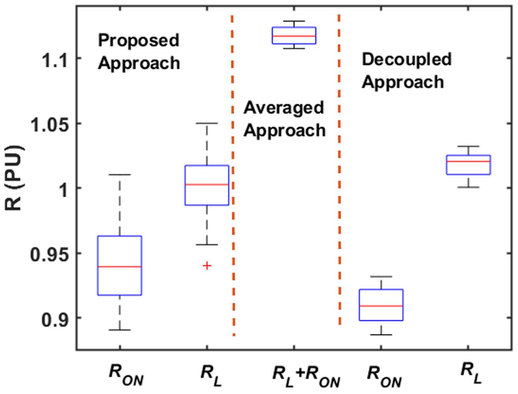

Fig. 8. $R_{L,a}, R_{ON,a}$ estimation approach comparison.

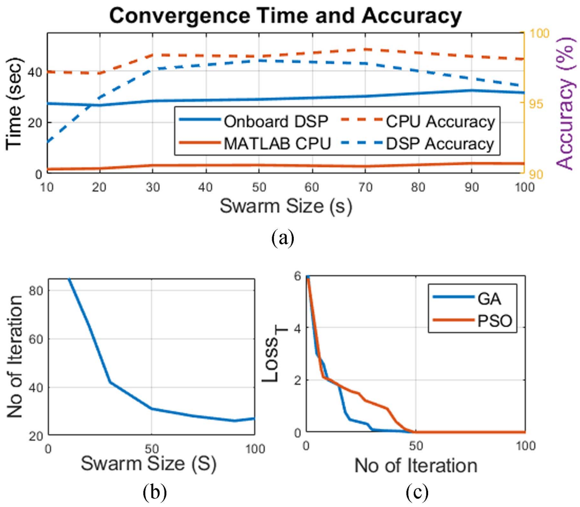

(a)

(b)

(c)

Fig. 9. (a) Onboard DSP vs CPU implementation of DT. (b) Impact of swarm size on convergence. (c) PSO versus GA comparison.

Notably, the R_{ON} estimation includes interconnecting and PCB resistances. Hence, the estimated R_{ON} has certain inaccuracies. However, it is an effective device indicator because it shows real-time variation trends. Any large fluctuation in R_{ON} values can effectively indicate system degradation. Furthermore, the standard deviation for $L_{1,2,3,4}$, C, and R_C are obtained to be as low as 4.2 µH, 3.2 µF, and 0.5 mΩ. Hence, it can be concluded that the precision error for this component estimation under normal conditions is deficient. However, the same is not true for $R_{ON,1,2,3,4}$ and $R_{L,1,2,3,4}$; the corresponding standard deviation values are 2.1 mΩ and 4.3 mΩ respectively. Hence, it can be inferred that the worst estimation spread was seen in the monitoring of the switch of phase legs. Considering that the ON-state resistance is vital in monitoring the health of a MOSFET, significant fluctuation makes the estimation of R_{ON} ineffective for indicating its health condition. One of the significant reasons why data spread in $R_{L,1,2,3,4}$ and $R_{ON,1,2,3,4}$ is high, as they are associated as a series component and individual assessment, are challenging for any heuristic or metaheuristic approach. For instance, as suggested in (8), it can be noticed that $R_{L,1,2,3,4}$ and $R_{ON,1,2,3,4}$ have the same impact on state variables like inductor channel current i_L. However, the impact of $R_{L,1,2,3,4}$ and $R_{ON,1,2,3,4}$ on V_o during switching state ON and OFF are different. This knowledge can be leveraged to evolve two possible ways to overcome these challenges.

1) *Averaging Approach:* Estimating $R_{L,i} + s_i R_{ON,i}$ instead of R_L or lumped device on resistance R_{ON}. This will allow the user to balance the error in both the parasitics as they are counterbalancing components, as suggested in (8). This approach was adapted by [5] and [6].
2) *Decoupling Approach:* This approach decouples optimization function into piecewise models based on device switching. The idea is only to estimate the $R_{ON,i}$ using the DT model when $s_i = 1$ considering R_L to be constant, whereas estimating $R_{L,i}$ using state equation during $s_i = 0$ considering $R_{ON,i}$ to be constant or previously obtained value. Notably, the estimation of R_L and R_C can be easily estimated without optimization using linear curve fitting of inductor and capacitor slopes during $s_i = 0$.

TABLE III
SENSITIVITY ANALYSIS: PSO VS GA

	L_{avg} =183µH	$R_{ON,avg}$ =15mΩ	$R_{L,avg}$ =150mΩ	R_C =3.5mΩ	C =240µF
σ_{PSO}	4.2 µH	2.1mΩ	4.3mΩ	0.5mΩ	3.2µF
σ_{GA}	3.8 µH	2.5mΩ	3.2mΩ	0.3mΩ	4.1µF

The approaches mentioned above are compared in Fig. 8. The result shown in Fig. 8 uses per unit comparison for lumped device on-resistance and inductor ESR to ensure fair comparison among estimations of three proposed methods. It can be observed that the average approach can be seen to have a very low spread compared to the proposed R_{ON} and R_L estimation. Hence, it can be concluded that the accuracy and precision of estimation can be improved using the averaging approach. However, this approach cannot decouple R_{ON} and R_L despite improved estimation precision.

A tradeoff solution between accurate, precise estimation, and decoupling ability of estimation can be achieved using the decoupling approach. Fig. 8, shows that the spread of estimation is higher compared to averaged approach but significantly lower compared to the proposed approach. It can be observed that the number of data points in the first and second quartile significantly increases in the estimation of both R_{ON} and R_L compared to the proposed approach. It is worth noting that the computation complexity of the decoupling approach is two times that of the proposed as well as averaging approach. Hence, the choice of approach remains to be a tradeoff between accuracy, precision, decoupling capability, and implementation/computational complexity.

Furthermore, the analysis is presented in Fig. 9(c) and Table III compares the descending process of using PSO and GA as optimizing heuristics. It can hence be concluded that the GA converged faster as compared to PSO for multiphase IBC.

TABLE IV
PARAMETER VARIATION CHART

Variation as % of actual value					
Component	$\Delta = 2\%$	$\Delta = 5\%$	$\Delta = 7.5\%$	$\Delta = 10\%$	$\Delta = 15\%$
L=183-$\Delta(H)$	179.3 (µH)	173.8 (µH)	169.2 (µH)	164.7 (µH)	155.5 (µH)
C=240-$\Delta(F)$	235.2 (µF)	228 (µF)	222 (µF)	216 (µF)	204 (µF)
R_C=3.5-$\Delta(m\Omega)$	3.57 (mΩ)	3.67 (mΩ)	3.762 (mΩ)	3.85 (mΩ)	4.02 (µΩ)
R_{ON}=15-$\Delta(m\Omega)$	15.3 (mΩ)	15.75 (mΩ)	16.12 (mΩ)	16.5 (mΩ)	17.2 (mΩ)

The average execution times observed for PSO and GA are 28.1 and 21.3 s, respectively. This is because each iteration of PSO converges faster than GA, but PSO requires more iterations for convergence. It shall be noted that the computational memory requirement of PSO is constant, whereas it continues increasing with each iteration for GA implementation. It shall be noted that swarm size and implementation platform can vary the number of iterations and time required for convergence criteria significantly, as suggested in Fig. 9(a) and (b). The results for sensitivity analysis are compared for two heuristic algorithms in Table III. It was noted that the estimation spread (σ_{PSO} and σ_{GA}) were highest for R_{ON} estimation considering the actual value of 15 mΩ. However, overall, GA performed better than PSO.

E. DT Robustness Analysis: HIL Emulation-Based Component Variation/degradation Scenario

This subsection looks closely into the ability of DT-based condition monitoring to estimate varied/degraded components. It is a nontrivial task to validate the condition monitoring ability to estimate varying components using accelerated testing. Hence, this article emulates the variation of components using a hardware-in-loop (HIL) system based on the Typhoon HIL 402 emulation platform. The components were varied in emulation, as suggested in Table IV. The robustness analysis is performed utilizing an emulated four-phase uncoupled IBC.

Environmental and operational conditions affect health indications and component levels. Certain condition monitoring approaches propose recalibrating sensors, components, or parameters [8], [13]. This can be a very time-consuming and impractical solution; when observed from an aspect of real-time, online, and nonintrusive nature of condition monitoring. The proposed method of testing component variation is analyzed using Table IV. Also, it is noteworthy that one component variation is emulated using the HIL system at a time. This ensures that error propagation due to other component variations/degradation does not impact the validation accuracy and precision.

The impact of varying components on condition monitoring estimation is as suggested in Fig. 10. The HIL-based degradation/variation emulation is executed on each component at various levels of variation one by one. Each time condition monitoring is set to converge 100 times before deriving the boxplot analysis. The estimation of various components under variation is represented in Fig. 10(a), (b), (d), and (e), whereas the impact of degradation on state variables i_L and v_c is given in Fig. 10(c) and (f).

It can be concluded from Fig. 10(a), (c), and (f) that the estimation spread for the capacitor under variation (240 µF to 204 µF) remained statistically constant, slightly increasing with variation. Also, i_L and v_c maximum values reduce with a reduction in the capacitor. Moreover, the charging–discharging constant of the dc link changes slightly, which causes errors in estimation. The same analysis holds true for R_C value estimation, as suggested in Fig. 10(b). However, variation of R_C does not vary the maximum value of v_c but significantly varies the charging–discharging constants, causing error in estimation, as suggested in Fig. 10(f).

The estimation of inductor under variation is from 183 µH to 155 µH. The estimation spread is statistically varying, randomly, with the spread being highest with a variation of 5%. Also, the i_L slope significantly varies due to any degradation in L, and v_c maximum values reduce with variation in the inductor without varying the charging–discharging time constant of the dc link. The boxplot analysis for R_{ON} has not been provided as it is observed that the impact of variation on R_L and R_{ON} shows a similar trend in estimation accuracy. It is noted that an increase in R_L lowers the i_L and v_c maximum values. However, this also explains why estimation of R_L and R_{ON} are very difficult as they make a minute variation/degradation on i_L. However, the variation v_c is helpful for a heuristic approach in the estimation of R_L. The same cannot be said for R_{ON} as it has a negligible impact on v_c.

Hence, it can be inferred that the only way to estimate R_{ON} is to utilize the decoupling approach and consider R_L to be a constant or a value computed by using the Loss_T calculation [in (14)] during the falling slope or in other words $s = 0$. Moreover, some of the critical points that can be concluded from this section is the loss calculation weights for voltage error should be kept higher for making DT highly sensitive to variation of R_L, C, R_C, L, whereas the weight for the inductor current loss calculation [in (13)] should be kept higher for making DT highly sensitive to variation of R_{ON}, L.

Despite perfect mathematical modeling, condition monitoring accuracy depends on objective function weights, memory constraints, application context, acceleration factor, swarm size, and maximum iteration for PSO. In addition, sensing/analog-to-digital converter (ADC) error, memory constraints, communication, and alternative approaches, can help in the estimation of health parameters. These practical insights are explained in detail in the next section.

V. PRACTICAL INSIGHTS ON DIGITAL TWIN IMPLEMENTATION

The proposed DT-based condition monitoring algorithm is based on squared error loss minimization between the physical system and the digital model. This multiobjective optimization is used to gauge the health of parameters/components. It is important to note that this health estimation is highly sensitive to variation in Loss_T. Hence, in order to achieve accurate estimation for this physics and statistical condition algorithm, it is paramount to ensure error-less sensing computation. The value of Loss_T can be impacted by multiple sources of signal processing and sensing error. This section takes a deep dive into

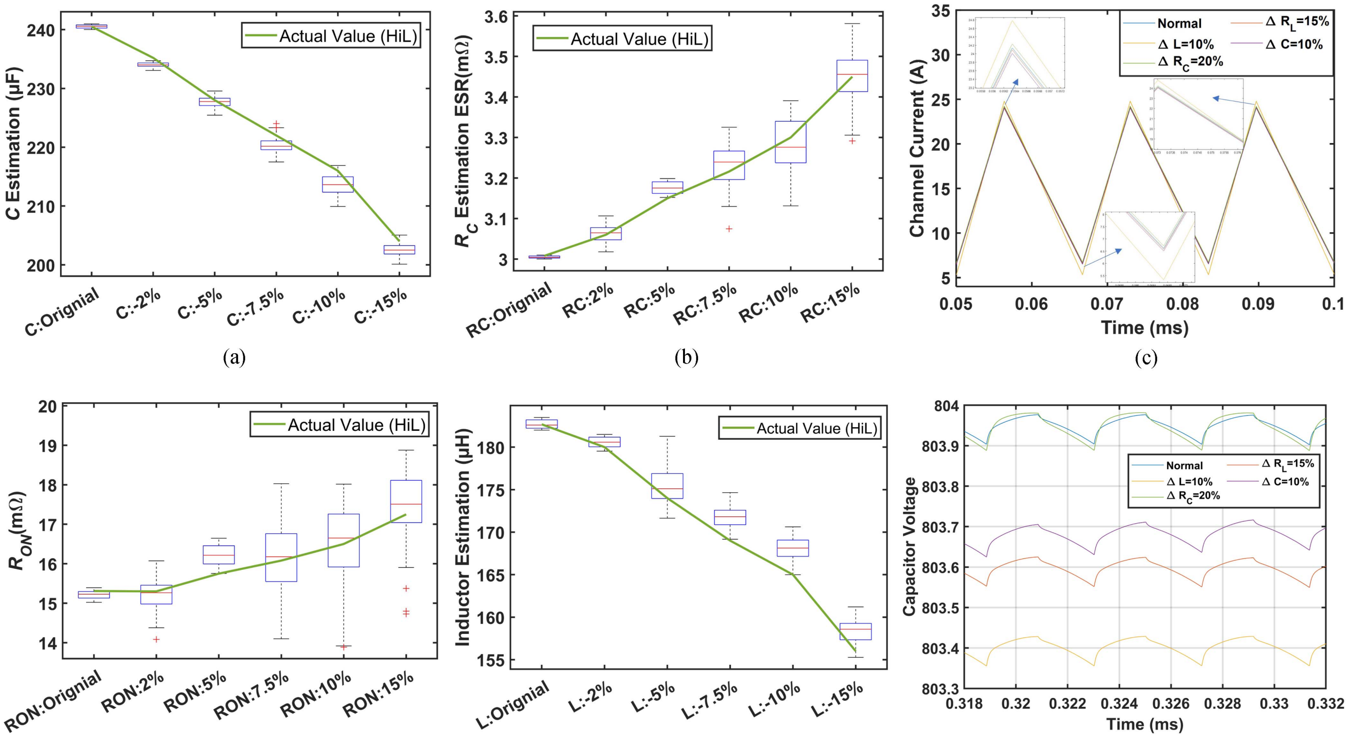

(a) (b) (c)

(d) (e) (f)

Fig. 10. Evaluation of robustness analysis and DT accuracy across different component cases as suggested in Table IV. Notably, the green line in the boxplots signifies the range of actual component values. (a) C variation: boxplot analysis. (b) R_C variation: boxplot analysis. (c) Impact of variation on state variable i_L. (d) R_{ON} variation: boxplot analysis. (e) L variation: boxplot analysis. (f) Impact of variation on state variable v_c.

the external factors impacting condition monitoring of health parameters.

A. Error Due to Analog Signal Reconstruction

Reconstructing nonbandlimited signals, such as triangular and sawtooth waveforms, poses a challenge. The inductor channel current of the inductor-based converter (IBC) exhibits a triangular waveform or a combination depending on switching states and phases. The Nyquist–Shannon sampling theorem, applicable to band-limited signals like sine waves, cannot be used to determine sampling criteria due to the theoretically infinite bandwidth of triangular signals. This article suggests determining the minimum sampling frequency based on the IBC's switching frequency, duty cycle, and operation states. The minimum bandwidth, referred to as BW_{min}, is calculated as follows:

$$BW\text{min} = \frac{2}{\min\limits_{j=1,2,..,S_s} (T(s_j))} \tag{17}$$

where S_S is number of switching states, $T(s_j)$ is time per switching state. For instance, for a simple buck converter with a duty period D and switching frequency f_{sw}, the BW_{min} as $2 * f_{sw}/D$ and $2 * f_{sw}/(1-D)$ for $D < 0.5$ and $D \geq 0.5$, respectively. Hence, the minimum step size h_{min} can be given by $(BW_{\text{min}})^{-}1$ This article strongly advocates selecting f_{sw} larger than, as suggested in (17). The maximum error due to the step size resolution of the current sensor can be given as

$$R_{\text{max}} = \frac{(I_{\text{max}} - I_{\text{min}}) * T_{\text{sampling}}}{2 * T_{SW}} \tag{18}$$

where I_{max} and I_{min} are maximum and minimum values of inductor current. T_{sampling} and T_{sw} are switching and sampling time selected. Similarly, amplitude quantization error gets added on top of R_{max} due to ADC circuit.

B. ADC Conversion Error

The ADC conversion noise is prone to multiple errors due to the metastable state of ADC at high frequency. These errors can be categorized as follows.

1) Quantization error [36].
2) Offset and gain error [37].
3) Synchronization error [38].

Quantization error (Q) consists of two components: 1) amplitude and 2) time quantization. Time quantization implies the ADC is unable to adjust its sampling frequency and interval during an active sampling window, thus missing out on crucial information, whereas amplitude quantization implies an error in the accuracy of the ADC due to resolution. For most practical cases, the accuracy error e is uniformly distributed in amplitude between $\pm\Delta/2$, where quantization step size Δ is given in (19), with a dynamic signal range of $2D$ (peak to peak) and an ADC resolution of K-bit [39]. Moreover, when interfacing with the

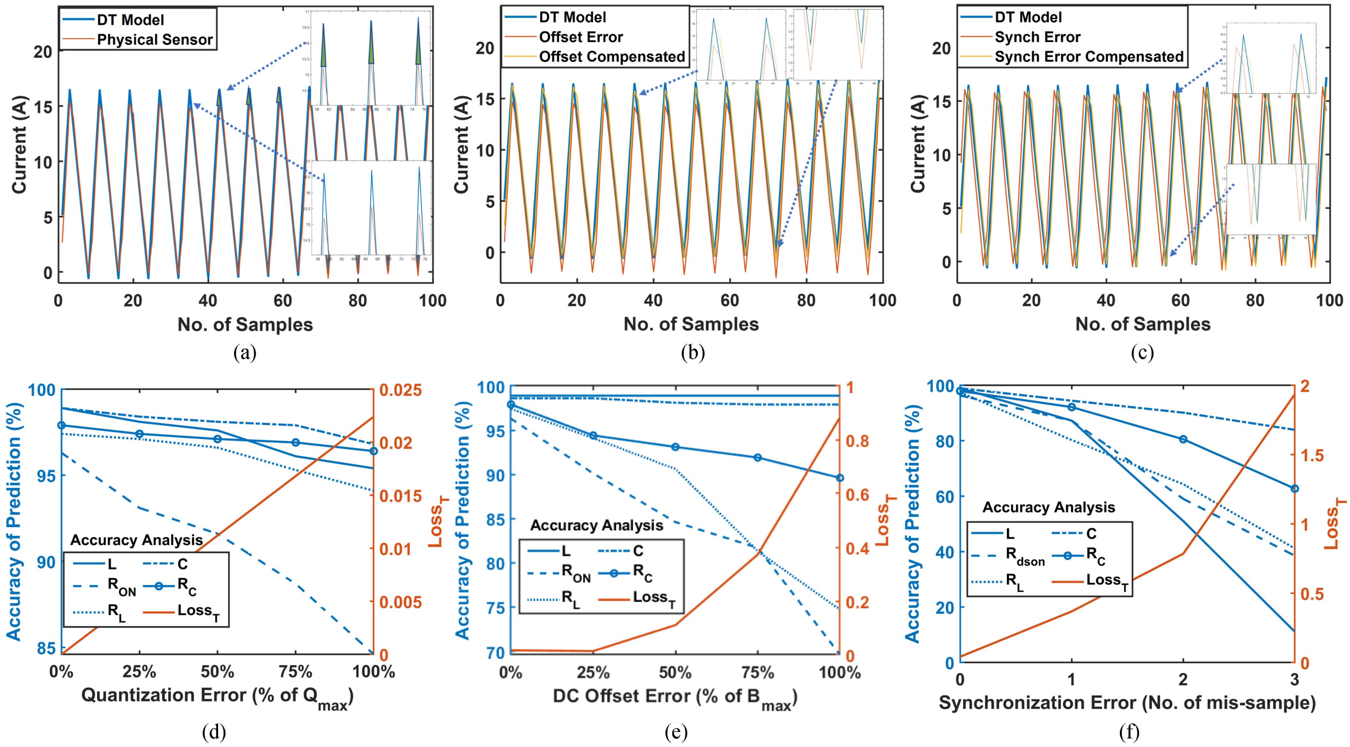

(a) (b) (c)

(d) (e) (f)

Fig. 11. Impact of practical sensing errors on DT model performance and accuracy of estimation of various parameters. (a) Quantization error. (b) DC offset error. (c) Synchronization error. (d) Impact of quantization error. (e) Impact of dc offset error. (f) Impact of synch error.

sensor, the maximum quantization and resolution errors add up to give a final error $Q_{\max}$, as presented in (20)

$$\Delta = \frac{2D}{2^K} = 2^{-(K-1)}D \tag{19}$$

$$Q_{\max} = R_{\max} \pm \frac{\Delta}{2}. \tag{20}$$

Fig. 11(a) illustrates the impact of $Q_{\max}$ on DT model performance. The sampled sensor data cannot capture inductor peak value due to $Q_{\max}$. This leads to the continuous error between DT model data and sampled sensor data, as signified in Fig. 11(a). The impact of varying amplitude quantization from 0 to $Q_{\max}$ can be seen in Fig. 11(d). The accuracy of estimation of R_{ON} and R_L is significantly impacted by quantization error. However, this does not impact the estimation of L, C. This is because quantization error mainly leads to an error in the peak value of the inductor current but has less impact on the slope of the inductor current or *RC* time constant for voltage waveform. This leads to a stable and robust estimation of L, C. This information may help the user to identify the type of error they are encountering during the practical implementation of condition monitoring.

This article suggests avoiding the impact of amplitude quantization error on Loss_T computation, where Loss_T is calculated as a function of sampled sensor data and DT model data. The methodology employed is by estimating $Q_{\max}$ for given sampling data and offsetting or compensating from Loss_T calculation every switching cycle. This approach forces the PSO to neglect all errors near the peak returned from the objective function and avoid amplitude quantization.

C. *DC Offset Error*

The sensor also generates offset and gain errors in addition to the amplitude quantization error. An offset error is a small preexisting output from the transducer due to uncertainties from the electronics and magnetic core retentively. Similarly, the ideal gain of the sensor is expected to be linear, but due to electronic uncertainty, the sensor does not always satisfy linearity. Similar errors are also seen due to the embedded platform but its error contribution is very small in comparison to sensor errors [36], [37].

The compound of all such errors can be defined as $B_{\max}$, which needs to be computed empirically during the initialization loop, as suggested in (21). $I_{L[DT]}$ is computed using the actual circuit parameter for only the initial iteration. This gives the condition monitoring the ability to compensate for dc offset error (B) for $B \leq B_{\max}$ dc bias compensation by comparing sensor and expected average values in i_{La} and V_o

$$B_{\max} = \mid \min(I_{L[\text{sensor}]}) - \min(I_{L[DT]}) \mid . \tag{21}$$

The impact of such offset error can be seen in Fig. 11(b). It seems like a dc offset on the current sensor. This error can be easily compensated in preprocessing. The dc offset error $B_{\max}$ can mainly impact the estimation accuracy of parameters R_{ON}, R_L, and R_C, as illustrated in Fig. 11(e). The PSO algorithm falsely identifies the dc bias as a change to the DT model, thus blaming all of the parameters related to R in the hope of countering the dc component. It is important to note that the impact of dc offset error can be much more than quantization error on estimation accuracy and DT model.

D. Signal Synchronization Error

Synchronization errors (S) greatly impact the DT's performance. Errors can stem from embedded circuits, sensing/communication delays, or sampling iterations. For instance, a synchronization error occurs at the 588th iteration when using 480.1 kHz instead of 480-kHz sampling for a 60-kHz signal. Fig. 11(c) shows the synchronization's impact on the DT model. Fig. 11(f) demonstrates reduced estimation accuracy (same order) for parameters L, R_{ON}, and R_L due to synchronization errors. C and R_C estimation remains relatively unaffected. To compensate, two methods are suggested. 1) Compute/compensate delay for sensing, communication, and time quantization. 2) Add a preprocessing synchronization algorithm, which can compensate up to $S_{\max} = \text{duty}{*}T_{SW}/T_S$. Fig. 11(f) compares compensated results to sensor data with synchronization error $S = 1$.

E. External EMI Noises and Cross-Talk

Close proximity DSP noise can also result in cross-talk and logic failures and failed condition monitoring. Three main solutions include optimizing power converter design, using shielded or fiber optic cables for CM chokes, and implementing H-field and E-field shielding. The current and voltage sensors in this work are connected to the control card via fiber optics, with a copper boxing grounding the shield for external E and H-field shielding.

F. Self-Evolving Preprocessing: Power Initialization and Adaptive Tuning

This article addresses the issue of parameter estimation inaccuracy caused by errors explained earlier, along with control or load variation. To mitigate these concerns, the proposed solution employs preprocessing steps using initialization data capture. These steps include tuning, error estimation, and sensor failure detection through pattern recognition-based techniques. This approach enables adaptive condition monitoring and ensures adaptability in the system.

1) Operating Condition Specific Initialization: This preprocessing-based initialization state is tasked to achieve the following.

a) Initialize DT algorithm in accordance to variation due to (control and load condition).

b) Adaptive tune error threshold Th based on operating condition.

c) Estimating switching states using sensor data instead of extracting gating signals from the on-board controller to ensure control nonintrusiveness.

First, available sensor data of i_L and V_o are utilized cyclically (after every optimization convergence), estimating duty (D), average operating power, the peak value of channel currents ($I_{L,\max}$), and the peak value of output voltage ($V_{o,\max}$). The estimation uses simple pattern recognition, as suggested in [40]. Second, the Savitzky Golay filtering [41] approach is used to achieve partial immunity from small signal noise.

The following information is passed on from these preprocessing steps. 1) Adaptive error threshold Th: Th determines convergence criteria. Now, for varying operating points the allowable errors have to be different to ensure optimal tradeoff between accuracy and time of convergence. Hence, is set to 3% of $(\sum_{a=1}^{N} I_{La,\max}^2 + V_{o,\max}^2)$, which is maximum possible value of Loss_T. 2) Initial values of $i_{L,a}$ and V_o to initialize RK ensure synchronization between DT and hardware data. 3) Duty (D), to ensure piecewise linearizing of state-space equation without using gating signals from controller unlike [5] and [6].

2) Error Tuning: Estimating and compensating for embedded and sensor errors is necessary for accurate parameter estimation. The following pattern-based error estimation techniques are used. 1) Quantization error (Q) is estimated using triangular approximation, as suggested in Fig. 11. 2) Dc offset error (B) is estimated by comparing dc values of DT signal and sensor data. 3) Synchronization error S is identified using the synchronization scheme presented in [42]. The time average compensation technique is used for all these errors if they are below $Q_{\max}$, $B_{\max}$, and $S_{\max}$, respectively.

3) Optimization Weight Tuning: In the event that one or more channel current sensors show increased errors or stop working in real time, This preprocessing step can be used to identify the failure by comparing error quantification to its theoretical maximum (theoretical). This step ensures minimum impact on monitoring or parameter estimation error due to this sensor integrity. As suggested in (22) and (23), optimization weights for (14) are inversely proportional to sensor integrity error. At the same time, if the error is more than the theoretical maximum error, the weights are floored to zero for that specific sensor/data. Similarly, adaptive relations can be set for PSO parameters λ, γ_1, and γ_2. Alternatively, if adaptive optimization is not required, α and β can be considered as 100 and 200, respectively. These constants were determined empirically using trial and error

$$\alpha_a = \frac{100}{I_{La,\max}}\left(1 - \max\left(\frac{Q_a}{Q_{\max}}, \frac{B_a}{B_{\max}}, \frac{S_a}{S_{\max}}\right)\right) \quad (22)$$

$$\beta = \frac{200}{V_{o,\max}}\left(1 - \max\left(\frac{Q}{Q_{\max}}, \frac{B}{B_{\max}}, \frac{S}{S_{\max}}\right)\right). \quad (23)$$

G. Embedded Design Constraint

The selection of a computational platform for DT applications poses challenges, particularly when considering the constraints of mobility and size. The proposed methodology design required an onboard processing unit equipped with: 1) multiple ADC channels to integrate the sensors, b) onboard UART communication interface, and c) serial peripheral interface protocol for control of hardware. The TI F28379D DSP was chosen as the preferred platform due to its ability to address the design requirements.

However, implementing a complex DT code is subjected to challenges from: 1) embedded computational capability, 2) time for convergence, and c) optimal tuning of DT parameters

(PSO and RK). Hence, these embedded challenges have been addressed in the following subsections.

1) Embedded Processor: Selection: In the context of a DT application and explained embedded constraints, the TI F28379D DSP is selected. Its core clock can reach a maximum frequency of 200 MHz. The processor's speed is not comparable to its desktop counterparts (GHz). However, this DSP is an onboard solution. It shall be noted that power electronic component degradation is a slow process (the general time frame is in terms of hours). Hence, the computational time of DSP is not critical, as it only serves as an online monitoring system. Furthermore, the DSP compensates for this by incorporating various peripherals to enhance its functionality, such as onboard ADC modules, a dual-core CPU with multithreading, user-configurable memory, etc.

The convergence time of the DT using PSO was analyzed using a MATLAB-based circuit simulator as well as a Typhoon HIL-based Python script. Convergence per health estimation cycle was observed to be around 3.2 and 5.7 s, computed using an inbuilt elapsed time stopwatch. However, the selected DSP takes around 28.3 s for the same. This is still fast enough for component degradation monitoring, as suggested in [5] and [6]. This convergence time heavily relies on the number of swarms, error gradient, and computation step size, as explained in the next section.

2) Embedded Processor: Memory Issue: The DSP memory has to store lots of data for the implementation of a DT. Each PSO iteration generates s sets of swarms, and the RK algorithm is executed s times per PSO iteration, producing $s \times N_p$ data points, where $N_p = 1/hf_{sw}$ is determined by $h \geq T_{\text{sampling}}$. The step size for our implementation was $h = 1/f_{\text{sam}}$, where sampling frequency $f_{\text{sam}} = 960$ kHz. However, it is important not to accumulate with each PSO iteration due to DSP memory overflow. The implementation overwrites the RK data as PSO iterates. The memory usage for the RK algorithm over a complete health estimation period is $s \times N_p$. And, PSO stores P_{best} and G_{best}, as suggested in (16).

The DT has been observed hanging or crashing during computation from memory leaking for $s \geq 80$. To resolve this issue, a custom linker file has been created to reallocate the data memory to a larger size to avoid memory leaking. It shall be noted that s should be determined considering the tradeoff between convergence time, memory requirement, and accuracy requirements [43].

3) Embedded Processor: Computational Power: To address this memory and convergence time issue, a solution involves employing multithreading [22]. This approach utilizes a second core that executes the same algorithm as the first, employing an identical swarm and iteration sizes. Since both cores share the same memory, the computation results, particularly the (Pbest) values obtained from each core, can be compared to determine the dominant (Pbest) at each iteration of the PSO. By implementing this approach, the DT can effectively double its swarm size while maintaining the overall computation time equivalent to that of a single core without drawbacks.

4) Embedded Processor: Hybrid Approach: Implementing the DT on a weaker MCU platform, such as TI's F28379S with a lower computational power rating, will likely result in convergence issues. When loaded onto the F28379D, the DT consistently crashes when increasing swarm size or max iteration of the PSO beyond a certain threshold. The processing power and memory size are insufficient for the DT to converge with larger swarm sizes or iterations. To address this, a hybrid approach in the PSO is explored apart from switching to a more powerful computational platform or applying the techniques described in the above subsection. PSO generates a group of swarms for each parameter of interest, those are, in the case of the IBC, values of L, R_L, R_C, R_{ON}, and C, this implies a total of s swarms for each parameter are being generated for each iteration. The hybrid approach allows calculating some parameters outside of the PSO algorithm, for instance, the inductor value L

$$L = \frac{v_L}{\frac{di_L}{dt}}. \tag{24}$$

Given a high precision sampling circuit, L can be calculated prior to the PSO individually at very high accuracy using (24), where v_L and i_L are the voltage across the inductor and current through the inductor, and di/dt is the slope of channel current. Utilizing a hybrid approach by calculating L outside of the PSO, 22.2% reduces the total number of swarms generated during each iteration. Moreover, estimating R_L and R_C using linear curve fitting of the decoupling approach can further reduce swarms generated during each iteration by 44.4%. This will also save significant memory. The only drawback of this approach is that a hybrid approach is an approach between heuristic optimization and deterministic computation that may lead to increased error. Hence, to choose this approach, a tradeoff needs to be considered.

VI. CONCLUSION

This article presents a system-level metaheuristic approach for condition monitoring of boost converters. The proposed methodology is applicable to multiphase IBCs with different inductor coupling strategies and modes of operation. Experimental validation is conducted using a four-phase IBC with coupled and reverse-coupled inductor strategies.

First, the methodology is validated by achieving identical waveforms of inductor channel current (i_L) and output voltage (V_o) between the physical IBC and its DT converter model under coupled and uncoupled scenarios. Second, parameter estimation is studied over 1000 iterations to assess the accuracy, precision, and robustness of condition monitoring. The estimation accuracy ranges from 98.6% for capacitance (C) estimation to 79.8% for R_{ON} estimation. Similarly, the estimation standard deviation is 3.2 µF for C and 4.3 mΩ for R_{ON}.

Lastly, the robustness of condition monitoring is observed under varied components, and the component variation is emulated using a HIL platform. It is found that estimation accuracy is achieved to be as high as 95.3% for C estimation and as low as 71.2% for R_{ON} estimation with a 15% variation case set. A similar trend is observed from the estimation standard deviation perspective, with standard deviation being 4.9 µF and 5.6 mΩ for C and R_{ON}, respectively.

This article suggests two solutions, namely, the averaged and decoupling approaches, for improving the estimation of R_{ON}. The averaged approach provides robust estimation accuracy but cannot distinguish between R_{ON} and R_L. The decoupled approach achieves estimation accuracy improvement of 9.4% and 11.3%, respectively, but at nearly twice the computational complexity and convergence time compared to the initial methodology. The article emphasizes practical considerations for implementing condition monitoring, including ADC conversion error, design constraints, sampling frequency, and cross talk. Hybrid condition monitoring solutions are proposed to reduce time complexity at the expense of accuracy. In conclusion, the proposed method offers a feasible, noninvasive, calibration-free, and practical solution for power converter condition monitoring without additional hardware circuits.

APPENDIX

A. *Impact of Coupling Coefficient on the Extended DT Model*

This article describes a four-phase IBC with a reverse coupled inductor strategy. Its schematic is represented in Fig. 12. This article provides an extended state-space modeling for multiphase IBC, which is valid for any inductor coupling strategy and any operation mode (CCM or DCM). The extended modeling can be realized using (3), (25)–(27) shown at the bottom of this page. Variable G_i refers to the decoupled self-inductor states of any phase leg, as suggested in (8) and (26), whereas $H_{m,n}$ refers to the impact of other phases on the state variable of that phase leg given in (25). It shall be noted $k_{i,j}$ is coupling between *i*th and *j*th channel inductors. Also, s_n or s_i refers to the switching state of MOSFET belonging to the *i*th phase. A complete coupling matrix is shown in (28) shown at the bottom of this page. This matrix applies to any multiphase IBC regardless of coupling strategy. The off-diagonal element of (28) represents the coupling coefficient of $H_{m,n}$ shown in (25). It shall be noted that k ϵ (-1,1).

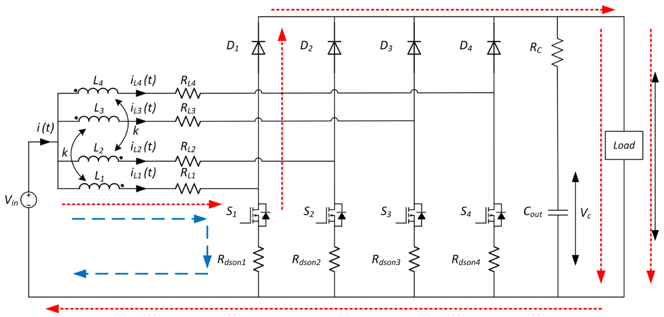

Fig. 12. Coupling strategy: multiphase IBC.

The extended state-space equation can be used for deriving the four-phases interleaved boost converter. For instance, case a), as suggested in Fig. 12, represents a four-phase interleaved boost converter, where all the channels are coupled. Hence, the

$$H_{m,n}=\bar{s_n}\left(\sum_{\substack{i_1=1\\ i_1\neq n\neq n}}^{N}\bar{s}_{i_1}k_{i_1,n}+\sum_{\substack{i_1=1\\ i_1\neq i_2\neq n\\ i_1<i_2}}^{N}\sum_{i_2=1}^{N}\bar{s}_{i_1}\bar{s}_{i_2}k_{i_1,n}k_{i_2,n}+\cdot+\sum_{\substack{i_1=1\\ i_1\neq\cdots i_{N-1}\neq n\\ i_1<\cdots<i_{N-1}}}^{N}\cdots\sum_{i_{N-1}=1}^{N}\bar{s}_{i_1}\bar{s_{i_2}}\cdots\bar{s}_{i_{N-1}}k_{i_1,1}k_{i_2,1}\cdots k_{i_{N-1},1}\right) \tag{25}$$

$$StateMatrix\ A=\begin{bmatrix}\frac{-1}{K_c}[G_1+H_{m,1}P] & \frac{-1}{K_c}[G_2+H_{m,2}\frac{P}{k}] & \cdots & \cdot & \sum_{\substack{i_1=1\\ i\neq 1}}^{N}\bar{s_i}P+\bar{s_1}Pk\\ \frac{-1}{K_c}[G_1+H_{m,1}\frac{P}{k}] & \frac{-1}{K_c}[G_2+H_{m,2}P] & \cdots & \cdot & \sum_{\substack{i_1=1\\ i_1\neq n}}\bar{s_i}P+\bar{s_2}Pk\\ \vdots & \vdots & \ddots & \vdots & \vdots\\ \frac{\bar{s_1}}{C}[\frac{R}{R+R_c}] & \frac{\bar{s_2}}{C}[\frac{R}{R+R_c}] & \cdots & \frac{\bar{s_N}}{C}[\frac{R}{R+R_c}] & \frac{\bar{-1}}{C}[\frac{1}{R+R_c}]\end{bmatrix} \tag{26}$$

$$InputMatrix\ B=\begin{bmatrix}\frac{1+k}{K_c} & \frac{-1}{K_c}(\bar{s_1}k+\sum_{\substack{i_1=1\\ i\neq 1}}^{N}\bar{s_i})\\ \frac{1+k}{K_c} & \frac{-1}{K_c}(\bar{s_2}k+\sum_{\substack{i_1=1\\ i\neq 2}}^{N}\bar{s_i}))\\ \vdots & \vdots\\ \frac{1+k}{K_c} & \frac{-1}{K_c}(s_{\bar{N}-1}k+\sum_{\substack{i_1=1\\ i\neq N-1}}^{N}\bar{s_i})\\ 0 & 0\end{bmatrix} \tag{27}$$

$$\text{Coupling Matrix}\ =\begin{bmatrix}1 & k_{1,2} & \cdots & k_{1,j}\\ k_{2,1} & 1 & \cdots & k_{2,j}\\ \vdots & \vdots & \ddots & \vdots\\ k_{i,1} & k_{i,2} & \cdots & 1\end{bmatrix}. \tag{28}$$

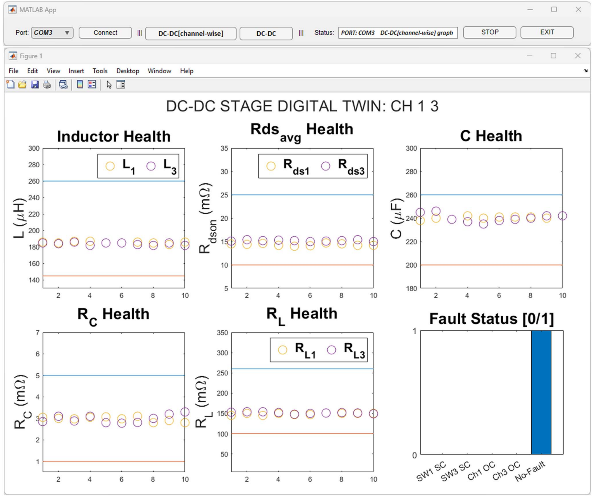
Port: COM3
Status: PORT: COM3 DC-DC[channel-wise] graph

Fig. 13. Channelwise graphical user interface.

first row of the coupling matrix will result in $[k_{1,1}k_{1,2}, k_{1,3}, k_{1,4}]$ or $[1, k, k, k]$ if all channels are having equal coupling coeffient k. Similarly, for case b) of Fig. 12, the first row of the coupling matrix will result in $[k_{1,1}k_{1,2}, k_{1,3}, k_{1,4}]$ or [1000], as the first channel is not coupled with any other channels. This coupling matrix plays a vital role in deducing state matrix from (25)–(28).

B. DT Report Out Strategy and Visualization

An onboard UART module serves as a channel, allowing the DT to broadcast to an external user interface. The uplink is active, with key parameters transmitted as a single packet at a fixed interval. Data are converted from floating point to hexadecimal format before transmission. To enable efficient data transmission, packet length depends on the monitored IBC phase count, increasing transmission size and time. Data integrity is maintained with header and footer inclusion in each packet.

For DSP broadcast reception, a UART receiver utilizes an off-the-shelf FTDI chip. The DT results are visualized through a MATLAB GUI that self-refreshes with new data at fixed intervals. The GUI interfaces with the terminal serial port, providing easy viewing of condition monitoring data by channel or system with a single button click. Fig. 13 illustrates channelwise information extracted from the DT. In addition, the DT enables monitoring of device degradation by estimating R_{ON} variation and distinguishing between temperature-related fluctuations and actual device degradation.

ACKNOWLEDGMENT

The team is grateful to Advanced Energy and Research Center and its Center Director James Acquaviva for support and testing facilities.

REFERENCES

[1] K. Choksi, Y. Wu, M. Ul Hassan, and F. Luo, “Evaluation of factors impacting reflected wave phenomenon in WBG based motor drives,” in *Proc. IEEE Int. Power Electron. Conf.*, 2022, pp. 736–740.

[2] S. Yang, D. Xiang, A. Bryant, P. Mawby, L. Ran, and P. Tavner, “Condition monitoring for device reliability in power electronic converters: A review,” *IEEE Trans. Power Electron.*, vol. 25, no. 11, pp. 2734–2752, Nov. 2010.

[3] E. Ribeiro, A. J. M. Cardoso, and C. Boccaletti, “Open-circuit fault diagnosis in interleaved DC–DC converters,” IEEE Trans. Power Electron., vol. 29, no. 6, pp. 3091–3102, Jun. 2014.

[4] G. Bhatti, H. Mohan, and R. R. Singh, “Towards the future of smart electric vehicles: Digital twin technology,” *Renewable Sustain. Energy Rev.*, vol. 141, 2021, Art. no. 110801.

[5] Y. Peng, S. Zhao, and H. Wang, “A digital twin based estimation method for health indicators of DC–DC converters,” *IEEE Trans. Power Electron.*, vol. 36, no. 2, pp. 2105–2118, Feb. 2020.

[6] A. B. Mirza, K. Choksi, S. S. Vala, M. K. Radha, M. S. Chinthavali, and F. Luo, “Cognitive insights into metaheuristic digital twin based health monitoring of DC-DC converters,” in *Proc. IEEE 24th Eur. Conf. Power Electron. Appl.*, 2022, pp. 1–7.

[7] H. Oh, B. Han, P. McCluskey, C. Han, and B. D. Youn, “Physics-of-failure, condition monitoring, and prognostics of insulated gate bipolar transistor modules: A review,” *IEEE Trans. Power Electron.*, vol. 30, no. 5, pp. 2413–2426, May 2015.

[8] U.-M. Choi, S. Jørgensen, and F. Blaabjerg, “Advanced accelerated power cycling test for reliability investigation of power device modules,” *IEEE Trans. Power Electron.*, vol. 31, no. 12, pp. 8371–8386, Dec. 2016.

[9] B. Ji et al., “In situ diagnostics and prognostics of solder fatigue in IGBT modules for electric vehicle drives,” *IEEE Trans. Power Electron.*, vol. 30, no. 3, pp. 1535–1543, Mar. 2015.

[10] X. Ye, C. Chen, Y. Wang, G. Zhai, and G. J. Vachtsevanos, “Online condition monitoring of power MOSFET gate oxide degradation based on miller platform voltage,” *IEEE Trans. Power Electron.*, vol. 32, no. 6, pp. 4776–4784, Jun. 2017.

[11] Z. Wang, B. Tian, W. Qiao, and L. Qu, “Real-time aging monitoring for IGBT modules using case temperature,” *IEEE Trans. Ind. Electron.*, vol. 63, no. 2, pp. 1168–1178, Feb. 2016.

[12] D. Xiang, L. Ran, P. Tavner, A. Bryant, S. Yang, and P. Mawby, “Monitoring solder fatigue in a power module using case-above-ambient temperature rise,” *IEEE Trans. Ind. Appl.*, vol. 47, no. 6, pp. 2578–2591, Nov./Dec. 2011.

[13] S. Dusmez and B. Akin, “An accelerated thermal aging platform to monitor fault precursor on-state resistance,” in *Proc. IEEE Int. Electric Machines Drives Conf.*, 2015, pp. 1352–1358.

[14] D. Xiang, L. Ran, P. Tavner, S. Yang, A. Bryant, and P. Mawby, “Condition monitoring power module solder fatigue using inverter harmonic identification,” *IEEE Trans. Power Electron.*, vol. 27, no. 1, pp. 235–247, Jan. 2012.

[15] B. X. Li and K. S. Low, “Low sampling rate online parameters monitoring of DC–DC converters for predictive-maintenance using biogeography-based optimization,” *IEEE Trans. Power Electron.*, vol. 31, no. 4, pp. 2870–2879, Apr. 2016.

[16] A. Soualhi et al., “Heath monitoring of capacitors and supercapacitors using the neo-fuzzy neural approach,” *IEEE Trans. Ind. Inform.*, vol. 14, no. 1, pp. 24–34, Jan. 2018.

[17] H. Soliman, H. Wang, B. Gadalla, and F. Blaabjerg, “Condition monitoring for DC-link capacitors based on artificial neural network algorithm,” in *Proc. IEEE 5th Int. Conf. Power Eng., Energy Elect. Drives*, 2015, pp. 587–591.

[18] A. Al-Mohamad, G. Hoblos, and V. Puig, “A model-based prognostics approach for RUL forecasting of a degraded DC-DC converter,” in *Proc. IEEE 4th Conf. Control Fault Tolerant Syst.*, 2019, pp. 312–318.

[19] M. Algreer, M. Armstrong, and D. Giaouris, “Active online system identification of switch mode DC–DC power converter based on efficient recursive DCD-IIR adaptive filter,” *IEEE Trans. Power Electron.*, vol. 27, no. 11, pp. 4425–4435, Nov. 2012.

[20] M. Ahmeid, M. Armstrong, S. Gadoue, M. Al-Greer, and P. Missailidis, “Real-time parameter estimation of DC–DC converters using a self-tuned Kalman filter,” *IEEE Trans. Power Electron.*, vol. 32, no. 7, pp. 5666–5674, Jul. 2017.

[21] J. H. Williamson, “Low-storage Runge–Kutta schemes,” *J. Comput. Phys.*, vol. 35, no. 1, pp. 48–56, 1980.

[22] “Launchxl-F28379d overview,” Texas Instrumments, Dallas, TX, USA, 2019, pp. 1–7.

[23] A. B. Mirza, A. I. Emon, S. S. Vala, and F. Luo, “An integrated magnetic structure for bi-directional two-channel interleaved boost converter with coupled inductor,” in *Proc. IEEE Energy Convers. Congr. Expo.*, 2021, pp. 5466–5470.

[24] A. J. Forsyth and G. Calderon-Lopez, “Sampled-data analysis of the dual-interleaved boost converter with interphase transformer,” *IEEE Trans. Power Electron.*, vol. 27, no. 3, pp. 1338–1346, Mar. 2012.

[25] D. Wu, G. Calderon-Lopez, and A. J. Forsyth, “Discontinuous conduction/current mode analysis of dual interleaved buck and boost converters with interphase transformer,” *IET Power Electron.*, vol. 9, no. 1, pp. 31–41, 2016.

[26] H.-B. Shin, J.-G. Park, S.-K. Chung, H.-W. Lee, and T. Lipo, “Generalised steady-state analysis of multiphase interleaved boost converter with coupled inductors,” *IEE Proc.-Electric Power Appl.*, vol. 152, no. 3, pp. 584–594, 2005.

[27] M. Roth and F. Gustafsson, “An efficient implementation of the second order extended Kalman filter,” in *Proc. IEEE 14th Int. Conf. Inf. Fusion*, 2011, pp. 1–6.

[28] J. Bene, I. Selek, and C. Hős, “Comparison of deterministic and heuristic optimization solvers for water network scheduling problems,” *Water Sci. Technol.: Water Supply*, vol. 13, no. 5, pp. 1367–1376, 2013.

[29] S. R. Sanders, “On limit cycles and the describing function method in periodically switched circuits,” *IEEE Trans. Circuits Syst. I: Fundam. Theory Appl.*, vol. 40, no. 9, pp. 564–572, Sep. 1993.

[30] R. Mazumder, A. Choudhury, G. Iyengar, and B. Sen, “A computational framework for multivariate convex regression and its variants,” *J. Amer. Stat. Assoc.*, vol. 114, no. 525, pp. 318–331, 2019.

[31] Z.-H. Zhan, J. Zhang, Y. Li, and H. S.-H. Chung, “Adaptive particle swarm optimization,” *IEEE Trans. Syst., Man, Cybern., Part B*, vol. 39, no. 6, pp. 1362–1381, Dec. 2009.

[32] D. S. Weile and E. Michielssen, “Genetic algorithm optimization applied to electromagnetics: A review,” *IEEE Trans. Antennas Propag.*, vol. 45, no. 3, pp. 343–353, Mar. 1997.

[33] A. B. Mirza et al., “Hardware design and implementation of a 75 kVA 3-D integrated intelligent power stage,” in *Proc. IEEE Appl. Power Electron. Conf. Expo.*, 2023, pp. 977–983.

[34] A. B. Mirza, X. Xu, A. I. Emon, F. Luo, and S. Chen, “A three-face utilized heat sink design for 3-D integrated 75kVA intelligent power stage (IPS),” in *Proc. ASME Int. Tech. Conf. Exhib. Packag. Integration Electron. Photonic Microsystems*, vol. 10, 2022, Art. no. V001T09A009.

[35] “C3M0016120D SiC MOSFET - Wolfspeed,” Wolfspeed, Durham, NC, USA, 2019. [Online]. Available: https://assets.wolfspeed.com/uploads/2020/12/C3M0016120D.pdf

[36] D. Chan and L. Rabiner, “Analysis of quantization errors in the direct form for finite impulse response digital filters,” *IEEE Trans. Audio Electroacoustics*, vol. 21, no. 4, pp. 354–366, Aug. 1973.

[37] S. Guan, J. A. Rice, C. Li, and C. Gu, “Automated DC offset calibration strategy for structural health monitoring based on portable CW radar sensor,” *IEEE Trans. Instrum. Meas.*, vol. 63, no. 12, pp. 3111–3118, Dec. 2014.

[38] Q. Li and D. Rus, “Global clock synchronization in sensor networks,” *IEEE Trans. Comput.*, vol. 55, no. 2, pp. 214–226, Feb. 2006.

[39] M. F. Wagdy, “Effect of ADC quantization errors on some periodic signal measurements,” IEEE Trans. Instrum. Meas., vol. IM-36, no. 4, pp. 983–989, Dec. 1987.

[40] H. Sira-Ramirez and M. D. deNieto, “A Lagrangian approach to average modeling of pulsewidth-modulation controlled DC-to-DC power converters,” *IEEE Trans Circuits Syst. I: Fundam. Theory Appl.*, vol. 43, no. 5, May 1996, Art. no. 427.

[41] D. Acharya, A. Rani, S. Agarwal, and V. Singh, “Application of adaptive Savitzky–Golay filter for EEG signal processing,” *Perspectives Sci.*, vol. 8, pp. 677–679, 2016.

[42] H. Minn, V. K. Bhargava, and K. B. Letaief, “A robust timing and frequency synchronization for OFDM systems,” *IEEE Trans. Wireless Commun.*, vol. 2, no. 4, pp. 822–839, Jul. 2003.

[43] O. Altinoz and H. Erdem, “Evaluation function comparison of particle swarm optimization for buck converter,” in *Proc. SPEEDAM*, 2010, pp. 798–802.

Kushan Choksi (Graduate Student Member, IEEE) received the B.Tech. degree in electrical engineering from Gujarat Technological University, Ahmedabad, Gujarat, India, in 2014, and the M.Tech. degree in power and control from the Indian Institute of Information Technology, Jabalpur, Madhya Pradesh, India, in 2017. He is currently working toward the Ph.D. degree in electrical engineering with the Department of Electrical and Computer Engineering, The Stony Brook University, Stony Brook, NY, USA.

He has two years of research experience with the Indian Institute of Technology, Gandhinagar, Gujarat, India, from 2017 to 2018, and the Indian Institute of Technology, Mumbai, Maharashtra, India, from 2018 to 2019, as Research Project Manager. He has recently completed an EMC internship with Tesla, Austin, TX, USA, working on system level compliance and prognosis, in 2022. His research interests include condition monitoring, diagnostics, prognostics, and control of electrical machine drives.

Abdul Basit Mirza (Graduate Student Member, IEEE) received the bachelor’s degree in electrical engineering (power) with honors from the University of Engineering and Technology, Lahore, Pakistan, in 2018, and the master’s degree with a concentration in MVDC breakers using WBG-based power electronics, in 2022, from Stony Brook University, Stony Brook, NY, USA, where he is currently working toward the Ph.D. degree in electrical engineering.

In 2022, he was a Research Intern with GE Global Research, Niskayuna, NY, USA. He is currently a Graduate Research Assistant and involved in research projects with the Oak Ridge National Laboratory, Oak Ridge, TN, USA, and Federal Aviation Administration, Washington, DC, USA. His research interests include system level design of high-density wide band gap-based power converters and electromagnetic interference and compatibility characterization.

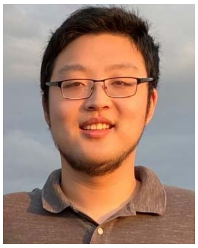

Austin Zhou (Graduate Student Member, IEEE) received the B.E. degree in electrical engineering from SUNY Stony Brook, Stony Brook, New York, US, in 2020, where he is currently working toward the Ph.D. degree in electrical engineering at the Department of Electrical and Computer Engineering at SUNY Stony Brook, Stony Brook, NY.

Prior to joining the Spellman High Voltage Lab (SHVL) at Stony Brook University in 2021, he worked as a Pathways Intern on projects under the supervision of NASA Johnson Space Center, Houston, Texas. Presently, he works in the domain of reliability studies including health monitoring, fault diagnosis and prognosis of power converters at the SHVL. His current research interests include the analysis, design, control, and modeling of power electronic converters.

Deepi Singh (Graduate Student Member, IEEE) received the bachelor’s degree in electrical engineering from Muzaffarpur Institute of Technology, Muzaffarpur, Bihar, India, and the master’s degree in power and controls from the Indian Institute of Information Technology, Jabalpur, Madhya Pradesh, India, in 2017. She is currently working toward the Ph.D. degree in electrical engineering with Stony Brook University, Stony Brook, New York, USA.

She has three years of teaching and research experience as an Assistant Professor with Government Engineering College, Bilaspur, Chhattisgarh, India, under the Technical Education Quality Improvement Project III of the World Bank. She has been involved in research projects with the Atlantic Marine Energy Centre, Durham, NH, USA, and Office of Naval Research, Arlington, VA, USA. Her research interests include the domain of distributed energy resources and their impeccable grid integration, advanced control methodologies, the augmentation of microgrid resiliency, and the intricate realm of real-time power system monitoring.

Masayuki Hijikata (Graduate Student Member, IEEE) received the B.E. degree in electrical engineering from Stony Brook University, Stony Brook, NY, USA, where he is currently working toward the M.S. degree in electrical engineering with an emphasis in power electronics.

He serves as a Graduate Research Assistant with the Spellman High Voltage Power Electronics Laboratory, Stony Brook University. His research interests include power quality and new passive filtering techniques for mitigating power system harmonics and reducing the effects of high-frequency PWM switching on the operation of ac motor drives.

Fang Luo (Senior Member, IEEE) received the bachelor's and Ph.D. degrees in power electronics from the Huazhong University of Science and Technology, Wuhan, China, and jointly from Virginia Tech, Blacksburg, VA, USA, in 2003 and 2010, respectively.

He was an Assistant Professor with the Electrical Engineering Department, University of Arkansas, Fayetteville, AR, USA, from 2017 to 2020, and a Research Assistant Professor with The Ohio State University, Columbus, OH, USA, from 2014 to 2017. He was a Visiting Ph.D. student, from 2007 to 2010, and then a Postdoctoral Researcher, from 2010 to 2014, with Virginia Tech, Blacksburg, VA, USA. He is currently an Empire Innovation Associate Professor and the Director of the Spellman High Voltage Laboratory, Stony Brook University (SUNY Stony Brook), Stony Brook, NY, USA, with his background in power electronics. His research interests include high power density converter design, high-density electromagnetic interference filter design and integration, and power module packaging/integration for wide bandgap devices.

Dr. Luo is also a Member of American Institute of Aeronautics and Astronautics and American Society of Mechanical Engineers. He was the recipient of the NSF CAREER Award.